2019

Upper-plate deformation of Late Pleistocene marine terraces in the Trinidad, California, coastal area, southern Cascadia subduction zone

Jason Scott Padgett
University of Rhode Island, jason_padgett@uri.edu

Harvey M. Kelsey

David Lamphear

Citation/Publisher Attribution

Padgett, J. S., Kelsey, H., & Lamphear, D. (2019). Upper-plate deformation of Late Pleistocene marine terraces in the Trinidad, California, coastal area, southern Cascadia subduction zone. *Geosphere, 15*(2), 1323-1341. https://doi.org/10.1130/GES02032.1
Available at: https://doi.org/10.1130/GES02032.1

Upper-plate deformation of Late Pleistocene marine terraces in the Trinidad, California, coastal area, southern Cascadia subduction zone

Research Paper

GEOSPHERE

GEOSPHERE, v. 15, no. 4

https://doi.org/10.1130/GES02032.1

16 figures; 3 tables; 1 supplemental file

CORRESPONDENCE: jason_padgett@uri.edu

CITATION: Padgett, J.S., Kelsey, H.M., and Lamphear, D., 2019, Upper-plate deformation of Late Pleistocene marine terraces in the Trinidad, California, coastal area, southern Cascadia subduction zone: Geosphere, v. 15, no. 4, p. 1323–1341, https://doi.org/10.1130/GES02032.1.

Science Editor: Shanaka de Silva
Associate Editor: Colin Amos

Received 3 July 2018
Revision received 16 January 2019
Accepted 8 April 2019

Published online 7 June 2019

Upper-plate deformation of Late Pleistocene marine terraces in the Trinidad, California, coastal area, southern Cascadia subduction zone

J. Scott Padgett[1,2], Harvey M. Kelsey[2], and David Lamphear[3]

[1]Department of Geosciences, University of Rhode Island, 9 East Alumni Avenue, Kingston, Rhode Island 02881, USA
[2]Department of Geology, Humboldt State University, 1 Harpst Street, Arcata, California 95521, USA
[3]Green Diamond Resource Company, PO Box 68, Korbel, California 95550, USA

ABSTRACT

Forming at sea level, uplifted shore platforms serve as long-term geodetic markers. The spatial distribution and elevation of marine terrace sequences offer insight into regional tectonics. In the Trinidad coastal area (California, USA), active tectonic processes reflect upper-plate deformation above the southern extent of the Cascadia subduction megathrust. A set of five uplifted and deformed Late Pleistocene marine terraces is preserved in the Trinidad region and provides an opportunity to analyze regional uplift, folding, and faulting. Using lidar imagery embedded within a GIS, we employ a surface classification model (SCM) that identifies uplifted marine terraces on the basis of their micro-topographical characteristics, i.e., low slope and low roughness. The SCM-based identification of marine terraces both supplements and verifies existing field mapping. We demonstrate the utility of the SCM, which can be applied to a variety of surface terrain analysis investigations that seek to identify smooth and/or rough terrain features, e.g., terraces and fault scarps. Age assignments for the five marine terraces, which range from 80 ka to <500 ka, are based on paleo–sea cliff geomorphology and soil development trends. Specifically, the steepest, highest, and most prominent paleo–sea cliff, which is associated with terrace number 3, is correlated to the long-duration sea-level highstand centered at 125 ka (marine isotope stage 5e), exemplifying a novel method in relative age assignment for Pleistocene geomorphic features. Based on these age assignments, the average maximum uplift rates in the Trinidad coastal area are ~1.0 m/k.y., and the average long-term uplift rate diminishes westward to ~0.4 – 0.5 m/k.y. on the downthrown side of the Trinidad fault. Based on analysis of deformation using the high-resolution lidar imagery of the marine terraces, the Trinidad hanging-wall anticline represents a fault propagation fold that ceased to be active when the associated reverse fault, the Trinidad fault, daylighted to the surface ca. 80–100 ka. Based on deformation tilts of a marine terrace with an assigned age of 200 ka, the Trinidad anticline has accommodated at least 1 km of shortening in the last 200 k.y., which represents at least 2% of the convergence of the Juan de Fuca plate relative to North America over the same time period. Overall, both the hanging wall and the footwall of the Trinidad fault show long-term positive rock uplift, which implies that the Trinidad anticline and fault are contained within the hanging wall of a deeper structure. Therefore, the Trinidad fault likely splays off of the Cascadia subduction zone megathrust or off of a deeper thrust fault that splays off of the megathrust.

INTRODUCTION

The southern Cascadia subduction zone accommodates convergence of the Gorda–Juan de Fuca plates with the North American plate (Fig. 1A). The northern California (USA) coastal landscape shows a variable coast-parallel, long-term uplift rate north of the Mendocino triple junction (Carver and Burke, 1992; Merritts and Bull, 1989, Kelsey and Carver, 1988). This variability in uplift rates is a product of local tectonic structures that have developed in the overriding North American plate (Kelsey and Carver, 1988; Clarke and Carver, 1992).

A sequence of uplifted marine terraces across a coastal landscape serves as a datum that documents both past changes in relative sea level and upper-plate deformation. A marine terrace is a relatively flat geomorphic surface underlain by a thin (~2–20 m thick) veneer of marine sediment that in turn overlies a shore platform strath. Shore platforms form during sea-level highstands. The inner edge of a shore platform, which is the junction of the platform and the sea cliff, is horizontal at the time of formation and therefore provides a paleohorizontal datum when shore platforms are uplifted (Bradley and Griggs, 1976; Lajoie, 1986). The formation of marine terrace inner edges is inherently linked to sea level, and therefore such features are sea-level indictors with an indicative range (elevation range of occurrence) bound by the regional wave-climate parameters (Rovere et al., 2016). The spatial distribution and elevation of marine terrace inner edges positioned along a coastal landscape are an effective means to detect regional uplift rates, faults, tilts, and folds along a coastal landscape (Bradley and Griggs, 1976; Lajoie, 1986; Kelsey and Carver, 1988; Merritts and Bull, 1989; Kelsey, 1990; Carver and Burke, 1992).

The focus of this research is the marine-terraced Trinidad, California, coastal area between the Mad River fault zone and the Big Lagoon fault (Fig. 1). The Trinidad coastal reach, which is near the southern end of the Cascadia subduction zone, is ~70 km north of the Mendocino triple junction. The Trinidad coastal reach is within the onshore expression of the Cascadia fold-and-thrust

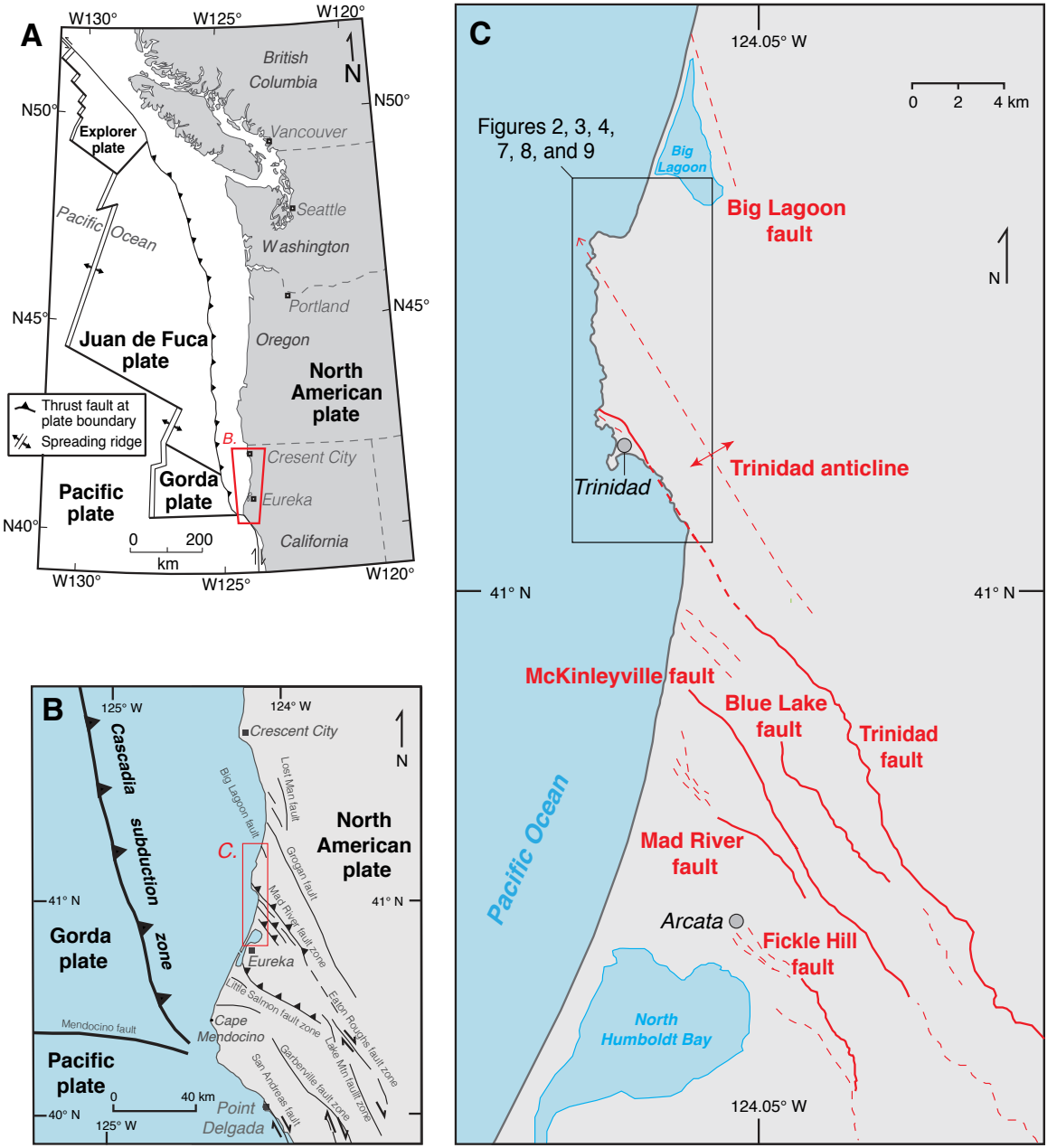

Figure 1. (A) Location of coastal northern California (USA) within a plate-tectonic context. (B) The two major, active upper-plate fault zones in the southern Cascadia subduction zone, the Little Salmon fault and the Mad River fault zone. (C) Mad River fault zone, consisting of five strands; the Trinidad fault is the northernmost strand.

belt (Clarke and Carver, 1992). The fold-and-thrust belt contains two major upper-plate fault zones: the Little Salmon fault zone south of the city of Eureka, and the Mad River fault zone north of Eureka (Clarke and Carver, 1992) (Fig. 1). The Trinidad fault is the northernmost fault of the Mad River fault zone (Fig. 1C).

High-resolution lidar data present the opportunity to refine the existing field mapping of uplifted marine terrace surfaces within the Trinidad coastal reach. Because the tectonically deformed Trinidad marine terrace sequence is one of the most extensive Late Pleistocene marine terrace sequences north of the Mendocino triple junction, the sequence provides an excellent opportunity to assess upper-plate deformation. Dense vegetation cover previously hampered geomorphological studies in the area, but the recent availability of bare-earth lidar imagery for the Trinidad coastal area (Figs. 2 and 3), the acquisition of which is further described below, provides a highly resolved landscape surface for terrace mapping and tectonic analysis.

The research objective is to assess, through mapping of uplifted and faulted marine terraces, upper-plate deformation caused by the Trinidad fault and associated folding. We use a high-resolution lidar data set, supplemented by soil development data, to characterize marine terraces and map upper-plate structures. The significance of our results is twofold. First, we demonstrate the efficacy of a surface classification model (SCM; Bowles and Cowgill, 2012) to distinguish marine terrace surfaces of different age and the proficiency of surface terrain analyses to characterize tectonic deformation patterns within lidar data sets. Second, we utilize our results of marine terrace deformation to infer style of deformation of underlying upper-plate faults and folds and ultimately how these structures play a role in accommodating convergence at this latitude on the Cascadia subduction zone.

GEOLOGIC SETTING

The Mad River fault zone represents the northernmost extent of onshore expression of the southern Cascadia fold-and-thrust belt. The Mad River fault zone consists of five principal northwest-trending, northeast-dipping thrust faults; from south to north, these faults are the Fickle Hill, Mad River, McKinleyville, Blue Lake, and Trinidad faults (Carver et al., 1983; Kelsey and Carver, 1988) (Fig. 1C). The Mad River fault zone offsets Pleistocene marine and fluvial sediments of the Falor Formation and Late Pleistocene fluvial and marine terraces near the coast. Kelsey and Carver (1988) estimated a net horizontal shortening along a northeast-southwest transect across the Mad River fault zone to be ~3.6 km.

The Trinidad fault and associated folding, which deform late Tertiary and Quaternary sediment over a ~10 km, NNW-trending trace length, represent a major upper-plate structure of the southern Cascadia subduction zone. The Trinidad fault, as the northern bounding fault of the Mad River fault zone, extends from the Little River to north of Trinidad, where the fault projects offshore (Carver et al., 1983). At the coast, the Trinidad fault displaces a marine terrace, and investigations by Woodward-Clyde Consultants (1980) determined slip

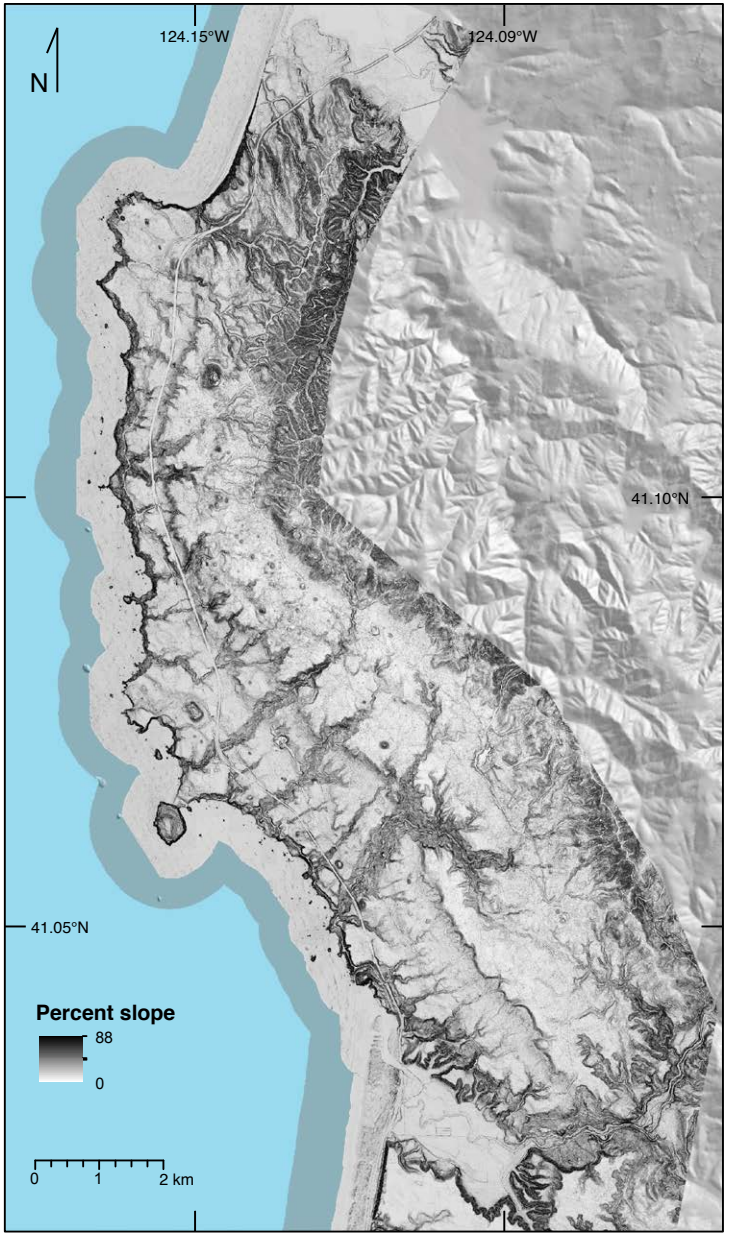

Figure 2. Lidar-derived slope map of the study area from Big Lagoon south to Little River, Trinidad coastal area, California (USA). A lidar digital elevation model is draped on top of the slope map with a 75% transparency setting.

rates of 0.2 mm/yr at a trench located near the town of Trinidad and 0.4 mm/yr based on a sea cliff exposure to the north-northwest. Clarke (1992) showed that the Trinidad fault and Trinidad anticline likely extend to the west and northwest across the continental shelf. The Trinidad fault scarp extends 4 km southeast from the sea cliff exposure; the fault scarp may extend even farther to the south, but the trace becomes uncertain (Woodward-Clyde Consultants, 1980).

Along strike to the south-southeast, the Trinidad fault transitions from a reverse fault to a strike-slip fault that is part of the transform margin. A regional geologic compilation that includes the Mad River fault zone (McLaughlin et al., 2000) shows that the Trinidad fault, south of latitude ~41°N, accommodates Mesozoic Franciscan rocks thrust over late Tertiary and Quaternary marine sediment. Farther to the south-southeast, the Trinidad fault merges with the Eaton Roughs–Lake Mountain fault zone, which is a strike-slip fault zone that is part of the San Andreas transform plate boundary (Kelsey and Carver, 1988) (Fig. 1B).

METHODS

Terrain Model

We employ a SCM that was designed to accurately locate marine terrace surfaces in thick vegetation in the elevation range of 100–450 m along the Mendocino and Sonoma coastlines in California (Bowles and Cowgill, 2012). The SCM detects marine terrace surfaces on the basis of topographic characteristics of low slope and low roughness. We apply the SCM to a similarly vegetated stretch of coastline in the vicinity of Trinidad (Figs. 1 and 2). The model utilizes a slope layer of the field area in a GIS (Fig. 2). Slope values ≥15° are eliminated, with 15° being the maximum slope of a marine terrace as described by Bradley and Griggs (1976). Roughness is assessed by the standard deviation of the slope (Frankel and Dolan, 2007), with larger values indicating greater roughness. Following Bowles and Cowgill (2012), we use a moving window of 3 × 3 cells to calculate the standard deviation of slope for each cell in the lidar-based digital elevation model (DEM), and truncated roughness values >~4.4. Including all values ≤4.4 resulted in incorporating 90% of the roughness values and excluding the highest roughness values. The selected slope and roughness layers are normalized and combined to produce the surface classification layer characterized by low slope and low roughness.

Lidar Acquisition and Analysis

In 2008, Green Diamond Resource Company (GDRCO, Seattle, Washington, USA; https://www.greendiamond.com/) hired Watershed Sciences, Inc. (based in Corvallis, Oregon; operating as a subsidiary of Quantum Spatial, Inc., https://quantumspatial.com/) to collect airborne lidar data across their land holdings, which encompasses the area of study. GDRCO lidar data were collected using a Leica ALS50 Phase II sensor mounted in a Partenavia P68 aircraft. The

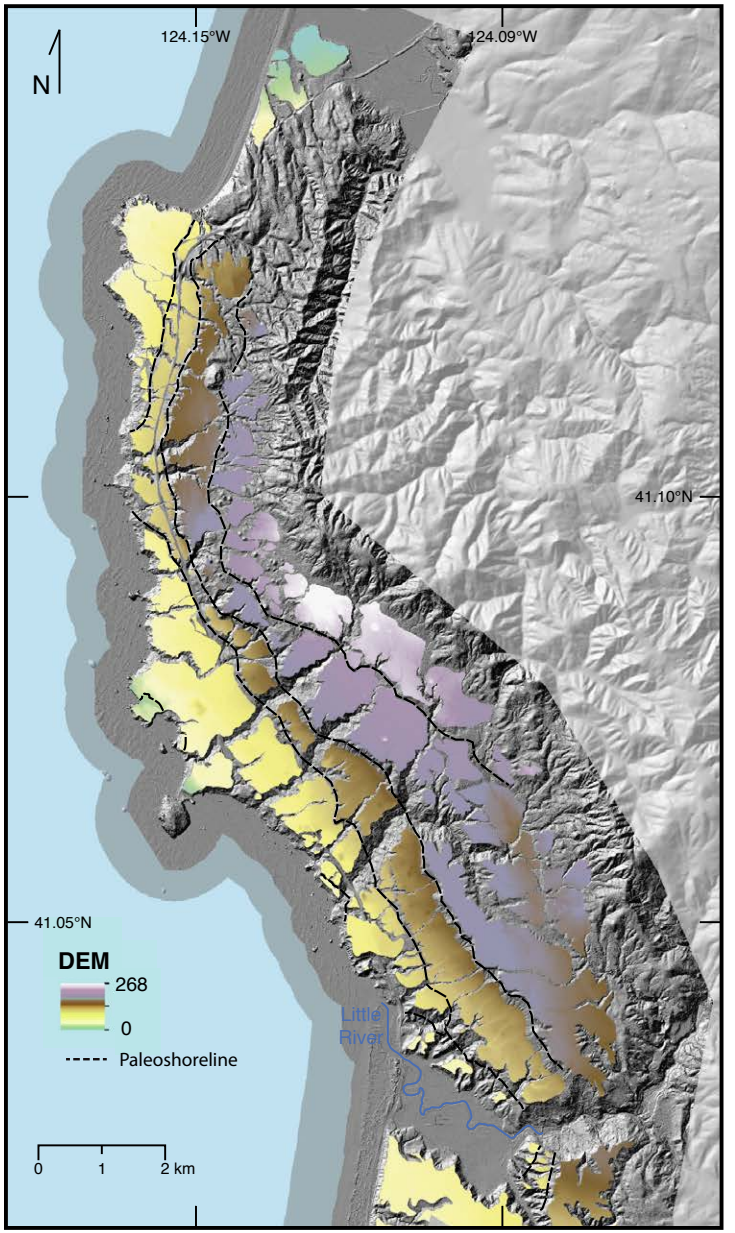

Figure 3. Elevation zones of mapped surfaces based on a lidar-derived digital elevation model (DEM), Trinidad coastal area, California (USA). Elevation zones range from blue (lowest) to white (highest).

aircraft was flown at 1000 m above ground level, and the Leica ALS50 Phase II system was set to collect ≥99,000 laser pulses per second. The field of view was limited to no more than ±8° tilt off from nadir, and a minimum of eight elevation points per square meter were required. These requirements necessitated multiple flyovers. The resulting dense point-cloud data set, assessed by the contractor, was reported to retain an accuracy of ±0.02 m, verified by real-time kinematic global navigation satellite system surveys in open areas. Ground points from the filtered point cloud were interpolated to a 1 m raster using a block kriging methodology developed by GDRCO.

Several tools and procedures in ArcMap (http://desktop.arcgis.com/en/arcmap/) are used to manipulate a lidar-based DEM as a basis to infer tectonic deformation of the uplifted marine terraces (Figs. 2 and 3). An elevation map for the terrace surfaces is created to display elevation trends within any one terrace tread and to show elevation differences between adjacent terrace treads (Fig. 3). From the elevation map, an aspect layer is created to query the slope-facing direction for the different surfaces at 1 m cell resolution (Fig. 4). A location map of soil data is presented in Figure 5 and a summary of the data is in Figure 6, each of which contributes to mapping and distinguishing the terraces (Fig. 7). We further evaluate the relation between surface weathering and terrace level by quantifying geostatistical surface parameters and compare averaged values of slope and roughness (standard deviation of slope) with a 3 × 3 kernel (Table 1). Moreover, a 5 × 5 kernel is used in order to eliminate the noise in the average slope values. Alongshore topographic profiles, at 1 m resolution, are constructed across each of the mapped surfaces from Big Lagoon south toward Little River (Fig. 8).

Soil Development Analysis

For the purposes of better characterizing the Trinidad marine terrace sequence, soil development trends provide a means to assess age relative to nearby marine terrace sequences with better age control. To assess soil development, we compile and analyze 62 soil descriptions on marine terrace surfaces within the Trinidad coastal area and to ~4 km south (Fig. 5). The U.S. Natural Resource Conservation Service (NRCS) shared copies of original field notes and laboratory reported data for 37 soil descriptions, which were collected for the northern Humboldt and Del Norte County soil survey (USDA–NRCS, 2018). Thirteen soil descriptions are derived from original field notes (R.M. Burke, 2011, personal commun.) that formed the basis for interpretations reported in Carver et al. (1985) and Carver and Burke (1992). Additionally, we describe soils at 12 sites. We combine these soil investigations in order to compile field-describable soil properties that are quantified within each soil investigation and are most representative of time-dependent soil development at a site (Burke and Birkeland, 1979; Birkeland, 1984; Carver and Burke, 1992; Kelsey and Bockheim, 1994). These properties, which include Bt (clay enriched) horizon thickness, depth to the Cox horizon (oxidized parent material), and maximum estimated clay content within the B horizon, change as a function of time and

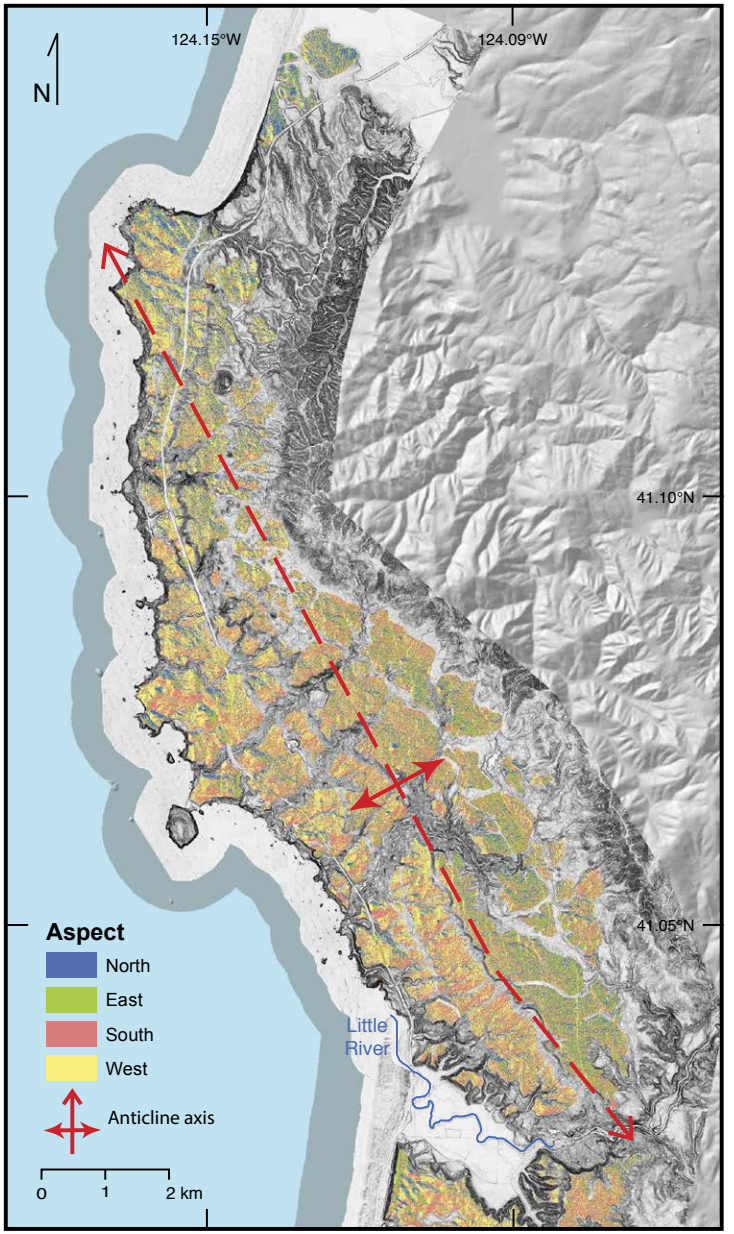

Figure 4. Lidar digital elevation model–derived slope aspect map for 1 × 1 m cells, Trinidad coastal area, California (USA). Blue—north-facing slope; green—east-facing slope; red—south-facing slope; yellow—west-facing slope.

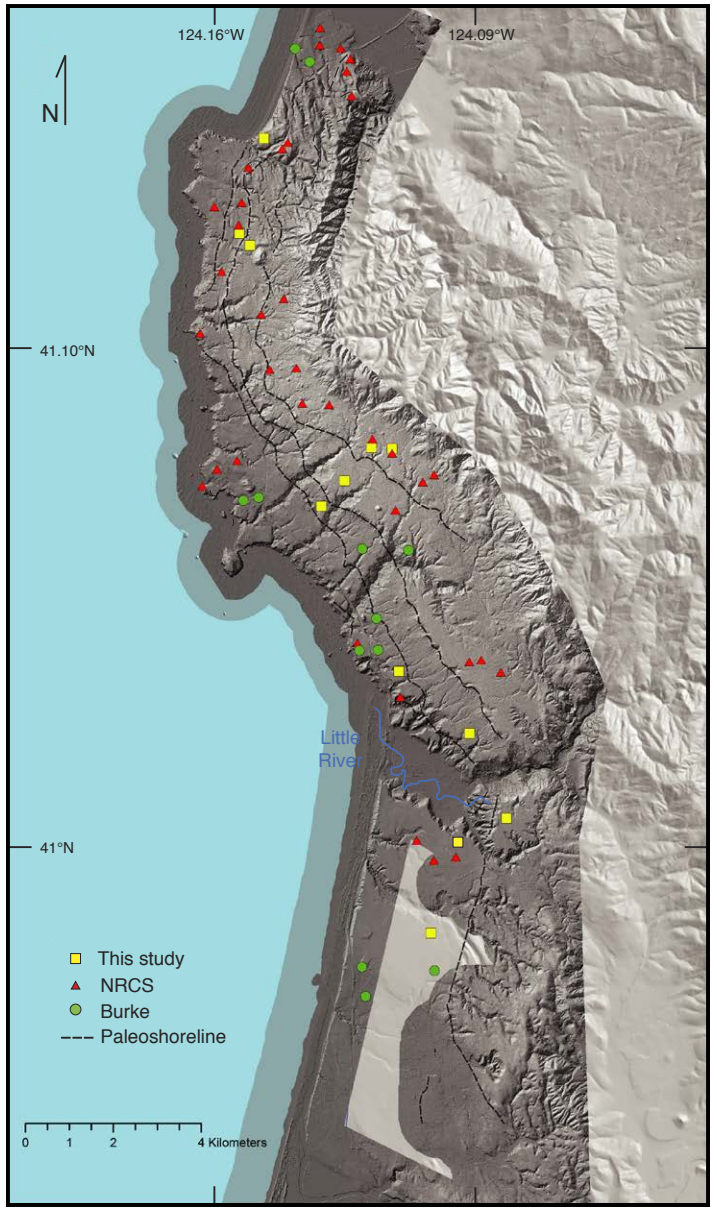

Figure 5. Pedon description locations layered above the lidar shaded-relief map and 10 m digital elevation model shaded relief, Trinidad coastal area, California (USA). Pedon description sources: yellow square—this study; red triangle—U.S. Natural Resource Conservation Service (USDA–NRCS, 2018); green circle—R.M. Burke (2011, personal commun.).

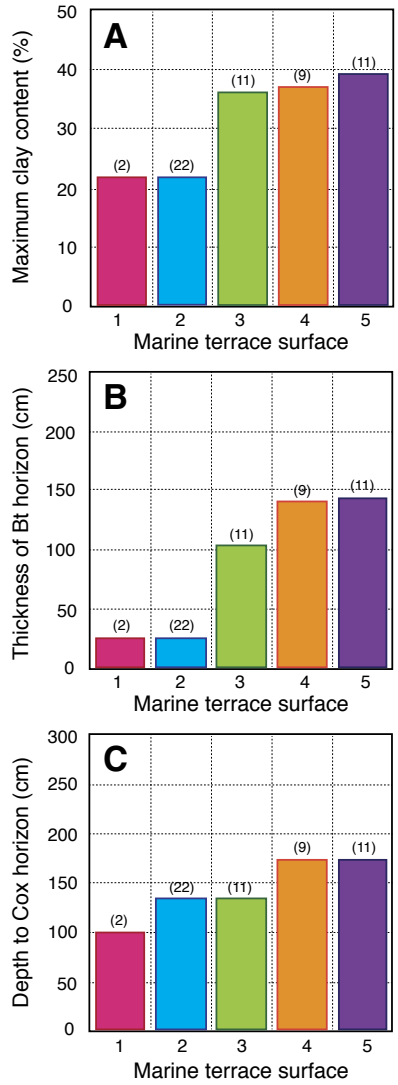

Figure 6. Histograms depicting time-dependent soil characteristics, Trinidad coastal area, California (USA). (A) Average maximum percent clay for soil profiles on a designated marine terrace surface. (B) Average thickness of the Bt horizon for soils on a designated surface. (C) Average depth to the Cox horizon for soils on a designated surface. The number within parentheses above each column represents the number of observations averaged for each column.

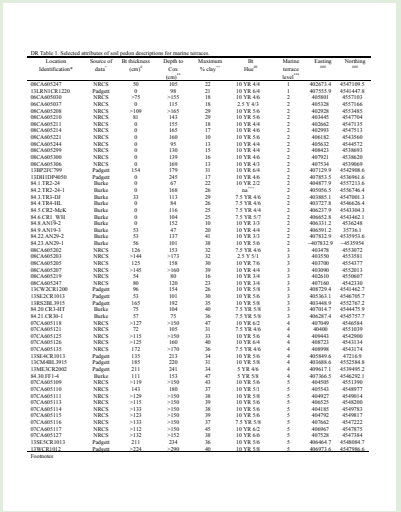

[1]Supplemental Information. Pedon attribute data are available for each soil description location. Please visit https://doi.org/10.1130/GES02032.S1 or access the full-text article on www.gsapubs.org to view the Supplemental Information.

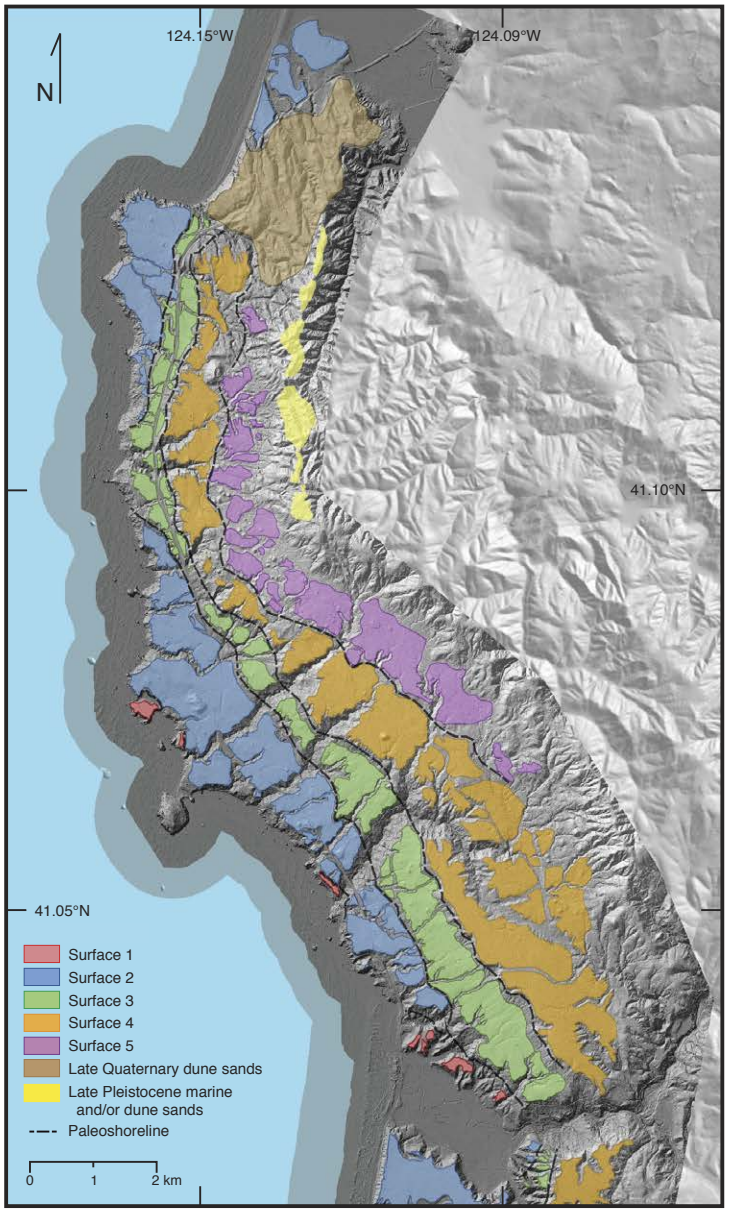

Figure 7. Mapped marine terrace surfaces (denoted 1, 2, 3, 4, and 5) within the study area, Trinidad coastal area, California (USA). Paleoshorelines (back edges of terrace surfaces) are delineated as dashed black lines. Other mapped geologic units in the study area include ridgetop Late Pleistocene marine and/or dune sands and late Quaternary dune sands south of Big Lagoon.

TABLE 1. MARINE TERRACE SURFACE GEOSTATISTICAL CHARACTERISTICS, TRINIDAD COASTAL AREA, CALIFORNIA (USA)

Terrace number	Mean slope (m)	SD of the mean slope	Mean slope (m) 5 × 5	SD mean slope 5 × 5	Roughness (m) 3 × 3	Roughness SD 3 × 3
1	9.946	10.802	8.755	9.637	2.543	3.194
2	10.363	11.214	9.107	9.745	2.695	3.084
3	12.032	9.417	10.580	7.996	2.942	2.496
4	11.687	9.247	9.784	7.800	3.084	2.448
5	13.022	10.222	11.030	8.509	3.405	2.750

Notes: SD—standard deviation. 5 × 5—5 by 5 meter cell window; 3 × 3—3 by 3 meter cell window. Roughness is calculated as the standard deviation of slope using a moving 3 × 3 meter cell window (Frankel and Dolan, 2007). See text for explanation.

have been used to distinguish marine terrace surfaces in southern Oregon and northern California (Carver et al., 1985; Kelsey and Bockheim, 1994; Kelsey et al. 1996). Where available and appropriate, we calibrate our field grain-size determinations with NRCS scientist and lab reports (USDA–NRCS, 2018). We conservatively assign ±10% errors to our and other field interpretations as well.

RESULTS

Terrace surfaces and inner edges became readily apparent using the SCM because it highlights areas with low slope and low roughness as well as eliminates areas with high slope and high roughness. Both the DEM and the SCM expose a sequence of five terrace surfaces and four inner edges along the Trinidad coastal area (Fig. 7). In Trinidad, the broadest mapped surfaces are surfaces 2 and 4, and the terrace surface of most limited areal extent is surface 1. The inner edge that separates surface 3 from surface 4 is the most prominent inner edge and is well exposed throughout the Trinidad coastal area (Fig. 2). The raster data sets also show that progressively higher-elevation terrace surfaces and inner edges are more eroded than the lower-elevation surfaces and inner edges. The geostatistical surface parameterization results indicate that the averaged slope and roughness values increase with terrace level, except for terrace levels 3 and 4, which are reversed (Table 1). The reversals for terrace levels 3 and 4 are consistent with the presence of the axis of the Trinidad anticline, which is mapped mostly on terrace level 4 (Fig. 4).

Soils

Pedon descriptions are available for soils on each of the five terrace surfaces (Figs. 5, 6; Supplemental Information, Table S1[1]). Each terrace surface has at least nine pedon descriptions, except for surface 1 that only has two because the surface tread is preserved only in three small fragments at the coast, and access issues limited the collection of soil data at each of the sites (Table S1).

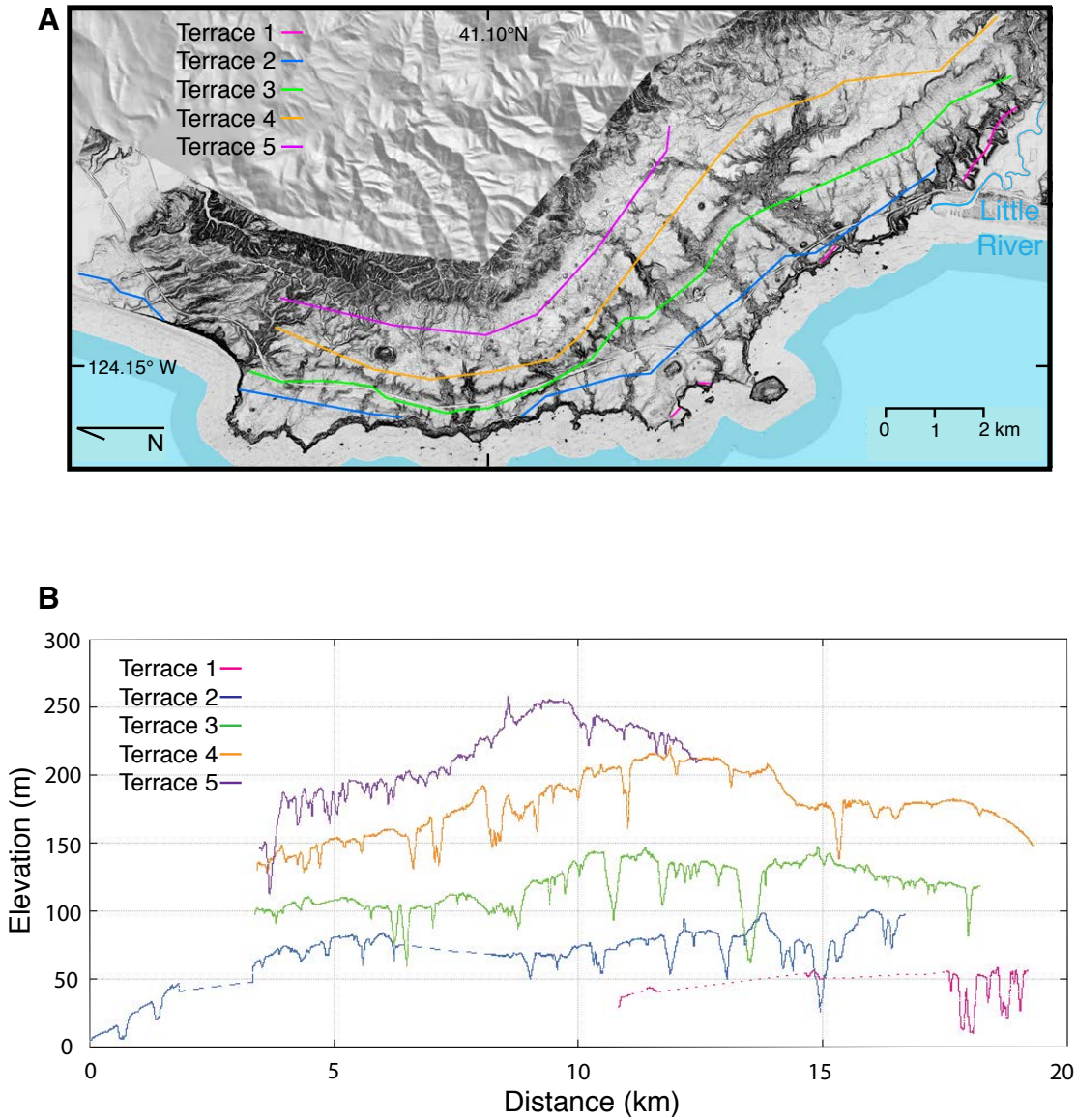

Figure 8. (A) Location of shore-parallel topographic profiles for marine terrace surfaces 1, 2, 3, 4, and 5 in the Trinidad coastal area, California (USA). Dashed lines are tie lines that connect a separated terrace surface. (B) Topographic profiles for locations shown in A, sampled at 1 m resolution. Red—surface 1; Blue—surface 2; green—surface 3; orange—surface 4; purple—surface 5.

On average, each of the three soil properties (maximum clay content, thickness of Bt horizon, and depth to Cox horizon) exhibited a greater degree of development going from the younger (lower-elevation) surface 1 to older (higher-elevation) surface 5 (Table S1; Fig. 6). The average maximum percent clay had values of 22%, 22%, 36%, 37%, and 39% from surface 1 to surface 5, respectively, showing an increase in average clay percent from the lower surfaces to the higher surfaces (Fig. 6A). The average thickness of the Bt horizon for surfaces 1 through 5 increases with terrace elevation, giving values of 25 cm, 26 cm, 104 cm, 141 cm, and 143 cm, respectively (Fig. 6B). Part of the reason for the exceptionally low average Bt horizon thicknesses on surfaces 1 and 2 is that most pedon description locations have B horizons that do not display an eluviation clay from overlying horizons; therefore, they do not qualify to be classified as Bt horizons. Consequently, a Bt horizon thickness cannot be measured (Table S1 [footnote 1]). The average depth to Cox horizon for surfaces 1 through 5 is 102 cm, 135 cm, 135 cm, 174 cm, and 176 cm, respectively, indicating an increase in Cox horizon depth from surfaces 1 to surface 5 (Fig. 6C). Overall, the combined soil properties data show an increase in soil development from surface 1 to surface 5.

Deformation of Marine Terraces

Assuming the terraces were originally planar and had an oceanward slope of 15 m/km (Bradley and Griggs, 1976), all terrace surfaces have been uplifted from the original elevation of formation and show additional tectonic deformation. Elevated junctions between paleo-platforms and paleo–sea cliffs (inner edges) serve as the foundational evidence for tectonic uplift. Further tectonic deformation is recognizable in the aspect map (Fig. 4), which displays the slope aspect on a per-cell basis with cell resolution of 1 × 1 m. When terraces were formed, the slopes faced west or west-southwest; and presently, a considerable amount of the Trinidad coastal area has surfaces that retain a dominant southwest- and west-facing slope (Fig. 4). However, surfaces 4 and 5 each have a significant amount of east-facing cells, reflecting back-tilt of these surfaces from the original seaward slope. In the northern Trinidad coastal area, surface 2 displays an abundance of north-facing cells (Fig. 4). Therefore, each terrace tread in the Trinidad coastal sequence has been exposed to uplift and tectonic deformation.

The lidar-derived DEM, with an applied false-color elevation symbology, depicts elevation changes along a single terrace tread as well as differences in elevation from surface to surface (Fig. 3). Individual surfaces in the Trinidad coastal area generally have lower elevation values in the north than in the south. Surface 4 is back-tilted, showing lower elevation values in the eastern extent than in the western extent (Fig. 3). Alongshore topographic profiles of each terrace tread (Fig. 8) display shore-parallel apparent tilts. These profiles are plotted along the middle of each tread in order to minimize the inclusion of colluvium shed off of the paleo–sea cliff deposited over the inner edge, and/or the inclusion of the eroded outer edge of the tread. The tread elevation profiles also document an antiformal structure that shows increasingly greater amplitude with each successively higher platform (Fig. 8B). There is an oblique intersection of the strike of the Trinidad anticline axis with the trend of the along-shore tread elevation profiles (Fig. 8), which produces an apparent southward shift of the anticline axis across decreasing terrace levels on the tread elevation profiles in Figure 8.

The terraces collectively show progressive folding of the Trinidad anticline. The folding is expressed by varying degrees and direction of terrace tilts as derived from the lidar data (Figs. 3, 4, 8, and 9). The clearly defined boundary between seaward tilt of surface 3 and the back-tilt of surface 4 defines the trend of the Trinidad anticline axis in the southern part of the Trinidad coastal area between the latitude of Trinidad Head south to the latitude of the mouth of Little River (Figs. 3, 4, and 8). Farther north, the abundance of north-facing cells reflects northern platform tilts on the northeastern, landward back limb of the Trinidad anticline (Fig. 4). The northern platform tilt is also exemplified along the Agate Beach cliff exposure (Fig. 10). Variable tilt directions across the mapped anticlinal axis are shown in Figure 9, which displays the average tilt direction for each mapped terrace polygon. Average tilt azimuth for the mapped marine terrace polygons on the east side of the Trinidad anticline is 184°, whereas 214° is the average for mapped marine terrace polygons on the west side.

The Trinidad fault (Figs. 11–15) is expressed along the seaward forelimb of the Trinidad anticline and has a trend subparallel to the axis of the Trinidad anticline (north-northwest) (Figs. 1 and 12). The high-resolution lidar imagery has also enabled more accurate mapping of the Trinidad fault. Two strands of the Trinidad fault occur north of the town of Trinidad where the fault offsets terrace surface 2 (Figs. 11–15). Trinidad fault scarp heights vary from as much as 17 m near the sea cliff to 10–12 m northeast of Trinidad on both strands (Fig. 11 and 13). The multiple strands merge to the south before becoming progressively more difficult to trace south of the town of Trinidad (Fig. 11).

DISCUSSION

Trinidad Fault and Trinidad Anticline

Suppe (1985) and Suppe and Medwedeff (1990) introduced the kinematic approach to describing the evolution of fault-propagation folds and summarized the typical characteristics of fault-propagation folding. Fault-propagation folds develop in the hanging wall of thrust faults that have not yet displaced the ground surface. During fault propagation, slip along a fault is not constant and decreases to zero at the tip. Folding of overlying material compensates for the lack of slip at the tip of the fault and growth of the fold is dependent upon propagation of the fault (Suppe and Medwedeff, 1990). Once the fault breaks the surface, fold propagation ceases or possibly continues at a much-reduced rate. Typical features of fault-propagation folds are distinct asymmetry with a steep, narrow forelimb and a wide, less-steep back limb. The fold tightens near the surficial fault expression, further suggesting that the fold and fault are intimately related. In general, fault-propagation folds are associated with thrust

faults with low displacements (Suppe and Medwedeff, 1990). The structural deformation model for fault-propagation folding of Suppe and Medwedeff (1990) uses kink-band geometries to approximate folding. Although other fault-propagation folding models preclude kink-band geometries and instead include progressive limb rotation, e.g., trishear (Erslev, 1991) and listric fault geometries (Amos et al. 2007), each require unique observations in order to correctly identify the style of deformation, e.g., measureable strata deformation and/or fault dips at depth or fault dips that increase toward the surface.

The Trinidad anticline, associated with the Trinidad fault, is an example of a fault-propagation fold. We acknowledge that trishear and listric fault geometries could explain the style of deformation observed in the Trinidad coastal area. However, the limited geospatial extent of the Trinidad coastal area and the lack of outcrops of either the Trinidad fault or marine terrace stratigraphy limit the ability to identify of the style of deformation beyond fault-propagation folding. The axis of the Trinidad anticline is subparallel to the trend of the Trinidad fault (Figs. 9, 12, and 13). The forelimb of the Trinidad anticline, i.e., the limb cut by the Trinidad fault, is the steeper limb and reflects upward propagation of the fault tip of the Trinidad fault (Fig. 13, 14, and 15). In cross section Y-Y′ (Fig. 15), tilts of surfaces 2, 3, and 4 are steeper than the original seaward slope, whereas surface 5 is markedly less tilted than the lower-elevation surfaces 2, 3, and 4. At the location of the cross section Y-Y′, the anticline axis is ~200 m from the back edge of terrace 4, and taken together, the terrace surfaces define the asymmetrical nature of the Trinidad anticline (Figs. 4, 8, 9, and 15). The general qualitative agreement between predicted fold shapes and the tilt of marine terrace surfaces provides support for the fault-propagation folding model of deformation for the Trinidad marine terrace sequence.

Marine Terrace Soils and Terrace Back-Edge Morphology: Implications for Terrace Age

In the Trinidad coastal area, soil properties change as a function of age for the five terrace surfaces (Table S1 [footnote 1]). The amount of soil development increases as surfaces increase in elevation. The average maximum percent clay steadily increases until reaching a maximum (Fig. 6). Averages of both the Bt horizon thickness and depth to Cox horizon increase progressively for surfaces 1–5 (Fig. 6). The progressive degree of soil development for surfaces 1–5 is consistent with soil development on other northern California (Mendocino County and Crescent City) and southern Oregon (Curry County) Late Pleistocene (80–500 ka) marine terraces (Carver and Burke, 1992; Polenz and Kelsey, 1999; Kelsey and Bockheim, 1994; Kelsey, 1990; McInelly and Kelsey, 1990).

The degree to which a sea cliff develops and retreats landward depends on the duration of the sea-level highstand, wave energy conditions, and offshore bathymetry (Anderson et al., 1999). Because the latter two variables are largely consistent at any given coastline from one highstand to the next, we use inner-edge morphology to infer relative duration of the four highstands that eroded the four sea cliffs.

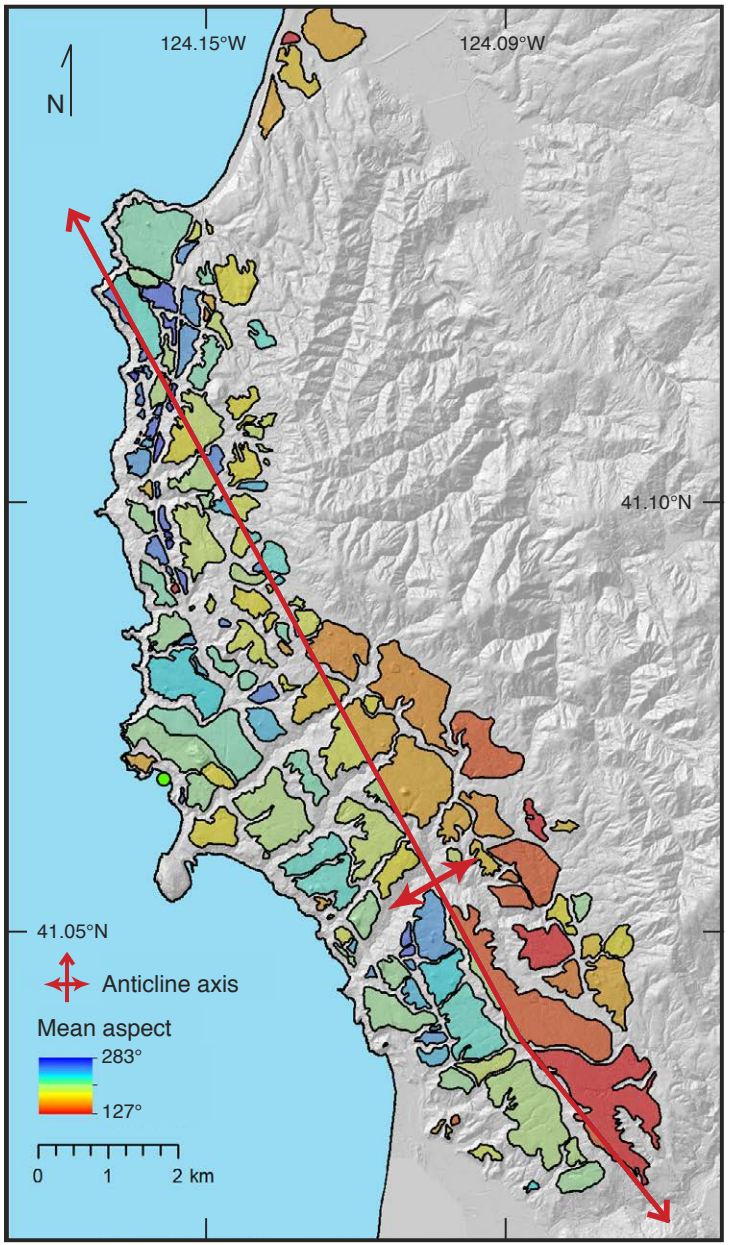

Figure 9. Mapped marine terrace polygons each showing a color-coded averaged tilt orientation, Trinidad coastal area, California (USA). Note the contrasting colors (i.e., contrasting average tilt) on either side of the hinge line of the Trinidad anticline.

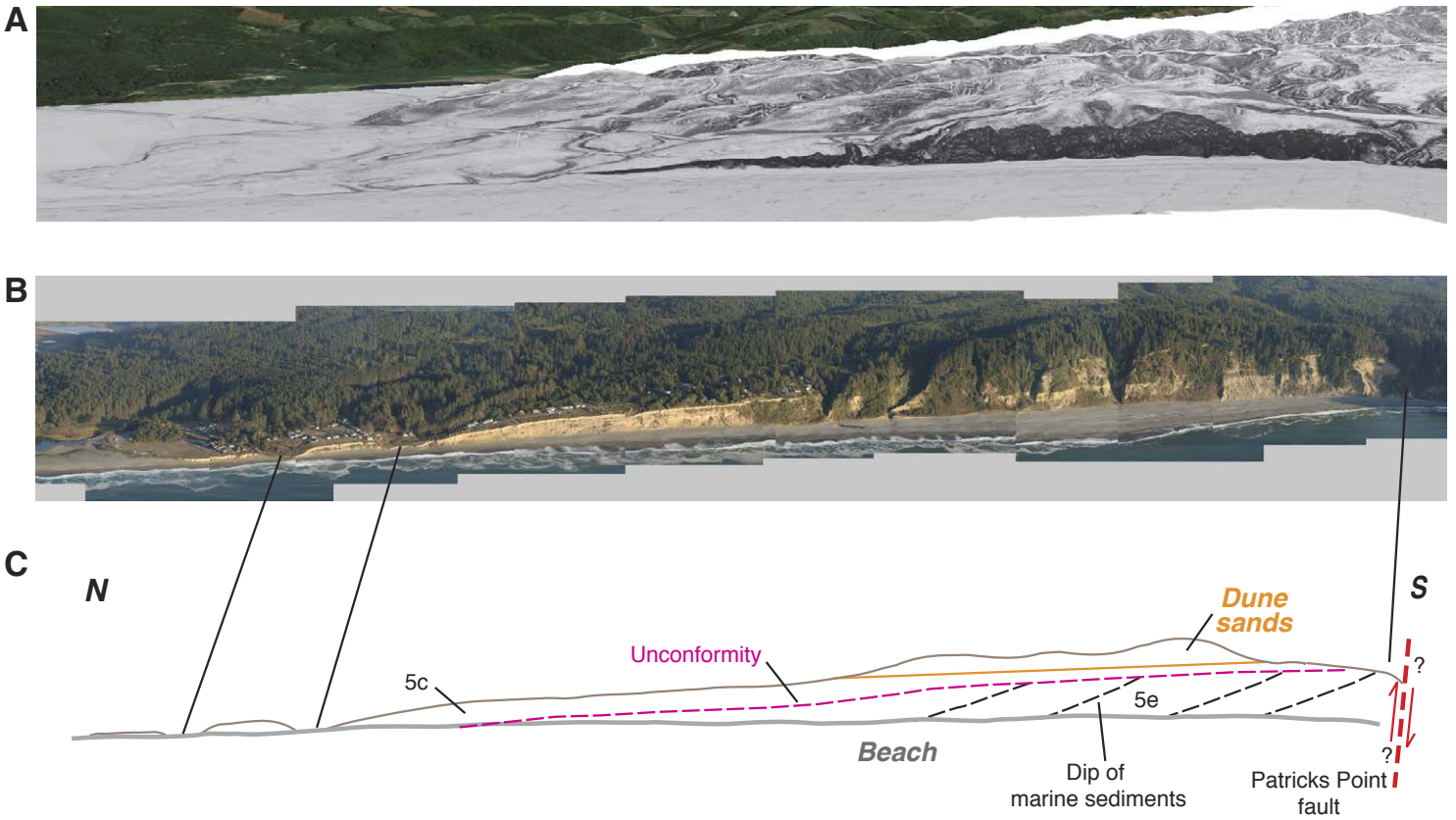

Figure 10. Big Lagoon to Agate Beach cliff exposure, Trinidad coastal area, California (USA). The outcrop, which is >100 m tall and ~3 km long, is composed of Late Pleistocene nearshore marine and beach sediments and contains a prominent unconformity between underlying marine isotope stage (MIS) 5e–age sediment and overlying MIS 5c–age sediment. (A) Obliquely rendered lidar view (view direction: ~N20E). (B) Oblique aerial view (view direction: ~N40E), images courtesy of California Coastal Records Project (www.californiacoastline.org) and captured in 2002. (C) Schematic sketch of outcrop, showing the prominent unconformity.

The longest-duration Late Pleistocene highstand was that of marine isotope stage (MIS) 5e (Shackleton and Opdyke, 1973; Chappell and Shackleton, 1986). Stirling et al. (1998) and Simms et al. (2016) reported that the MIS 5e sea-level highstand occurred ca. 128 ± 1 ka to ca. 116 ± 1 ka and 129–119 ka, respectively. A prominent inner edge should have been cut by the MIS 5e sea-level highstand and should be more pronounced than those cut by subsequent highstands. For instance, Muhs et al. (2002) documented a prominent inner edge on the Eel Point terrace, the MIS 5e inner edge, on the west coast of San Clemente Island in southern California. Several studies in central and southern coastal Oregon also reported a significantly larger MIS 5e paleo–sea cliff relative to the other paleo–sea cliffs associated with Late Pleistocene marine terrace sequences (Kelsey, 1990; Kelsey and Bockheim, 1994). Therefore, considering the last interglacial period, the sea-level highstand likely to have produced the most definitive Late Pleistocene inner edge is that of MIS 5e.

The most recognizable inner edge within the Trinidad coastal area is the inner edge that separates surface 3 from surface 4, and therefore we infer that this inner edge formed during the MIS 5e highstand (Figs. 2, 7, and 15).

Soil observations and a single marine terrace age determination, both in south coastal Oregon, are not inconsistent with the Trinidad terrace 3 being the MIS 5e terrace. The lowest three marine terraces in northernmost California (Polenz and Kelsey, 1999) and south coastal Oregon (Kelsey, 1990; Muhs et al., 1990; Kelsey and Bockheim, 1994; Muhs et al. 2002) have been interpreted as the three MIS 5 terraces (MIS 5a, 5c, and 5e). Furthermore, the lowest terrace in south coastal Oregon at Coquille Point has a U-series age of 80 ka (MIS

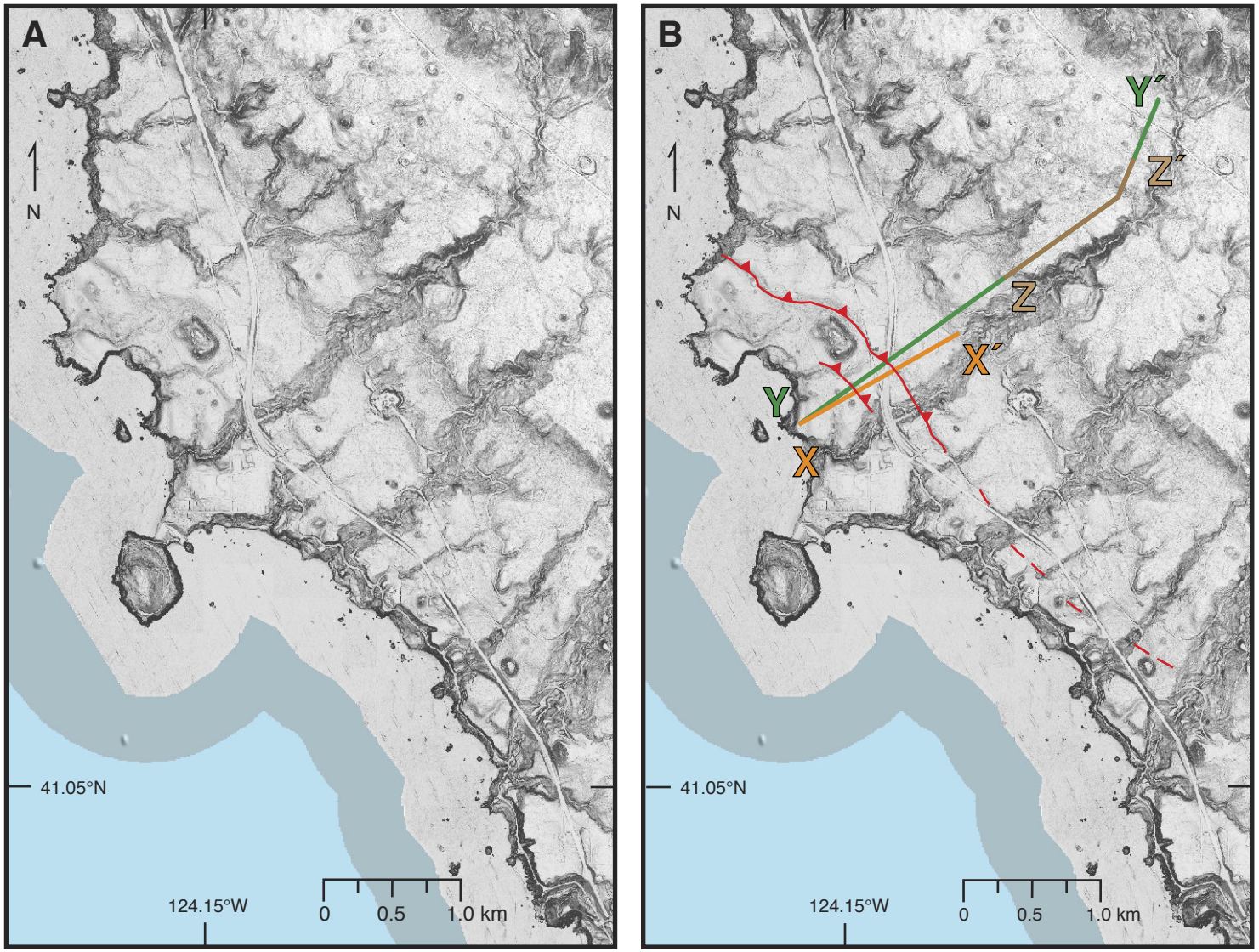

Figure 11. (A) Slope map of the area around Trinidad Head, Trinidad coastal area, California (USA). (B) Mapped interpretation of the Trinidad fault scarp. Also delineated is the location of the topographic profiles X-X′, Y-Y′, and Z-Z′ (see Figs. 14, 15, and 16).

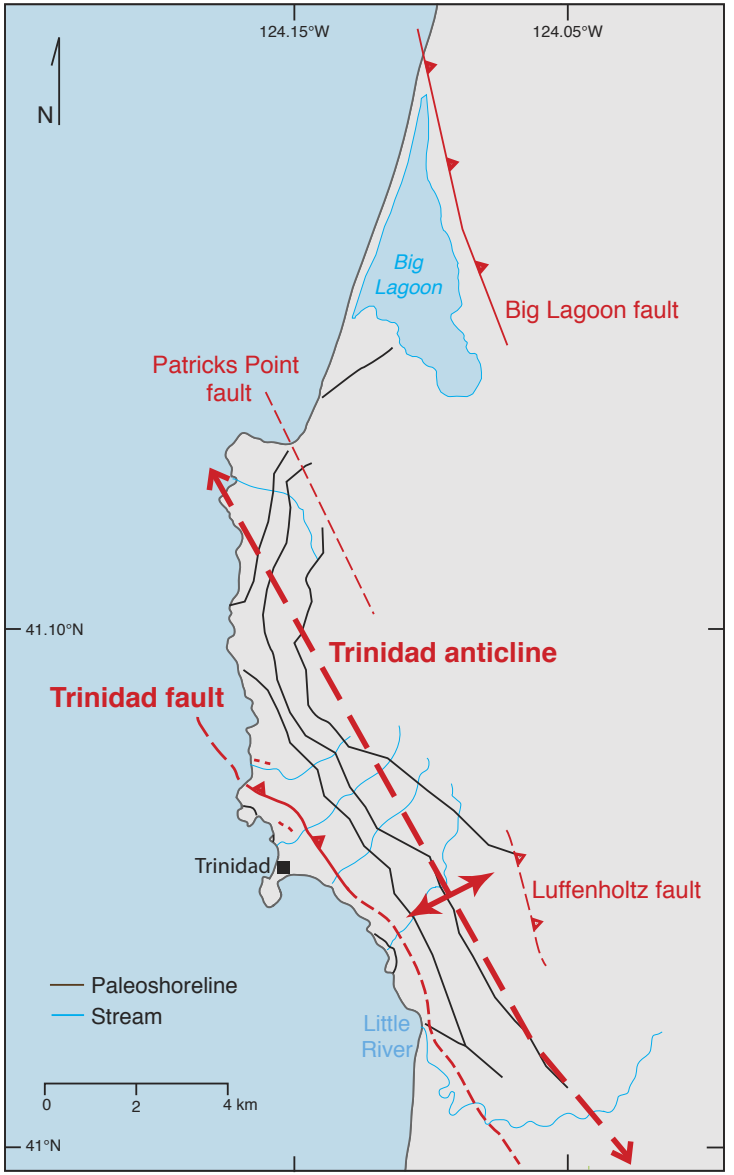

Figure 12. Tectonic map of the Trinidad coastal area, California (USA).

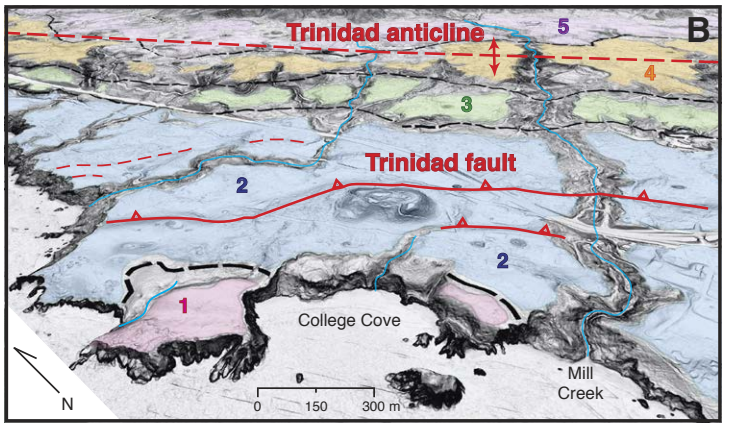

Figure 13. (A) Northeast oblique aerial view, north of the town of Trinidad, California. Image is a lidar-derived slope map loaded into Google Earth as a .kmz file. (B) Mapped interpretation, with marine terrace surfaces 1, 2, 3, 4, and 5 indicated.

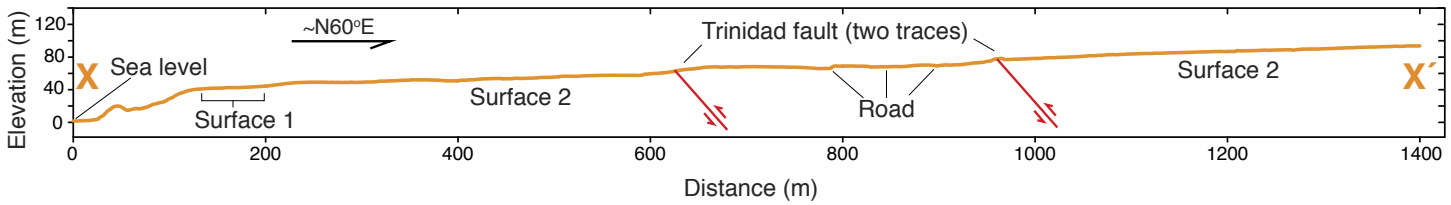

Figure 14. Northeast-trending topographic profile X-X′ (see location in Fig. 11), presented with no vertical exaggeration, showing two fault scarps that offset the marine terrace 2 surface.

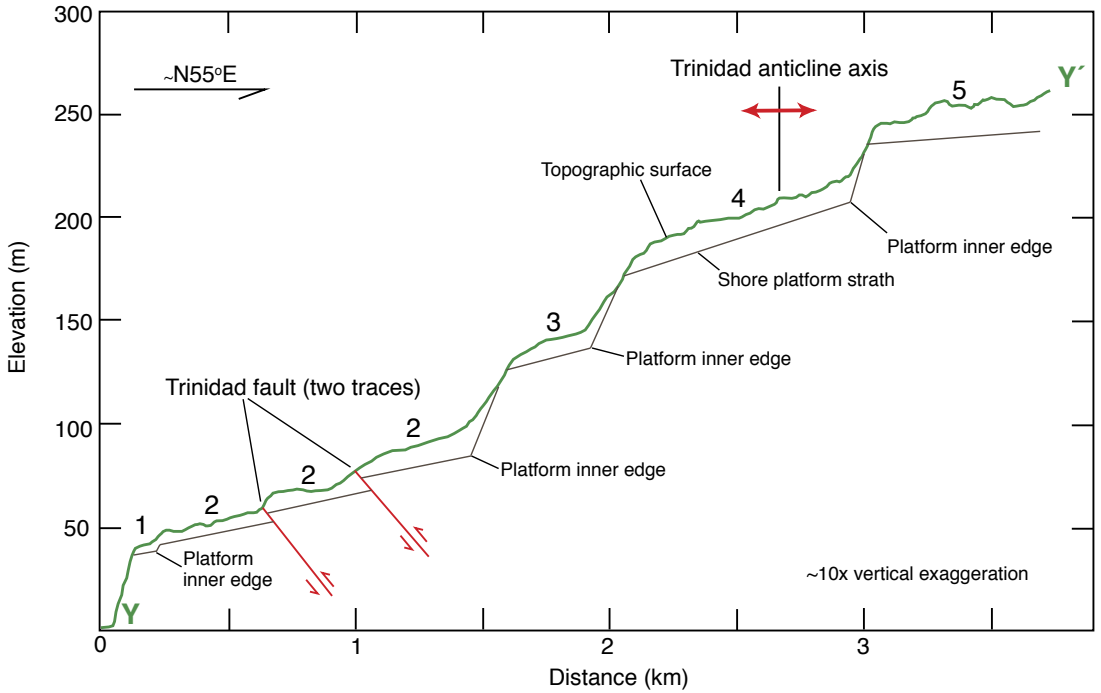

Figure 15. Northeast-trending topographic profile Y-Y′ (see location in Fig. 11) from which maximum long-term uplift rates were calculated for marine terrace surfaces 1, 2, 3, and 4. For each surface, the corresponding present elevation of the platform inner edge was taken to be the elevation of the inner edge below a specified sediment cover thickness. The inferred thickness, specific for each terrace, is outlined in Table 2.

5a) (Muhs et al., 1990). Therefore, we infer that ages of 84 ka, 106 ka, and 125 ka for MIS 5a, 5c, and 5e, respectively (Simms et al., 2016; Shackleton and Opdyke, 1973; Chappell and Shackleton, 1986), are the most appropriate assigned ages for marine terraces 1, 2, and 3 in the Trinidad coastal area. In accordance with the above inference, then marine terrace 4 may have been formed during the MIS 7 highstand. The age of relative sea-level fall from the MIS 7 highstand is estimated to be 190–200 ka based on chronostratigraphy constructed from high-resolution oxygen isotope stratigraphy (Martinson et al., 1987). Therefore, for the purposes of constructing uplift and deformation rates, we assign an age of 195 ± 5 ka to the time of relative sea-level highstand termination at the end of MIS 7.

Marine Terrace Uplift Rates

Uplift-rate calculations based on marine terraces require data on the age of the sea-level highstand at the time of formation of the terrace, the elevation of the highstand that formed the inner edge of the shore platform, and the present-day elevation of the inner edge. The present-day elevation of a raised inner edge must be inferred by subtraction of the known or estimated thickness of the cover sediments. In the Trinidad coastal area, thick vegetation precludes observation of the thickness of cover sediment above the shore platform. However, averages of cover sediment thicknesses are available from northernmost California and southern Oregon where shore platform unconformities and cover sediments are exposed (Table 2). Because the tectonic setting, wave regime, and coastline morphology in northernmost California and southern Oregon are similar to those of the Trinidad area, average thicknesses of cover-bed sediment in Table 2 are employed to estimate the range of thickness of cover-bed sediment on marine terraces in the Trinidad coastal area.

Mean sea level is the control on the formation elevation of a marine terrace inner edge; therefore, marine terrace inner edges are sea-level indicators. Rovere et al. (2016) suggested that the indicative range (the elevation range over which a sea-level indicator occurs) of a marine terrace inner edge, relative to mean sea level, has an upper limit of regional storm-water swash height (SWSH) and a lower limit of average wave height depth of breaking (DB). In order to quantify the indicative range of marine terrace inner edges along the Trinidad coastal area, we assume that the modern wave-climate parameters are similar to those that were present over the time periods of terrace formation, and that the wave-climate conditions are similar to those of Oregon, where SWSH = 7.8 m and DB = 2.7 m (Tillotson and Komar, 1997; Allen and Komar, 2006; Ruggiero et al., 2010). Therefore, the indicative range for each marine terrace inner edge along the Trinidad coastal area is 5.1 m.

In order to estimate tectonic uplift rates derived from sea-level highstand markers, corrections for glacial isostatic adjustment (GIA) must be considered when assigning past sea-level highstand elevations (Simms et al., 2016). Local responses to GIA and polar melt signatures can contribute to departure from the global eustatic signal. Creveling et al. (2015) and Creveling et al. (2017) demonstrated significant geographic viability in GIA from global geophysical models that incorporate the background ice-age cycle signal, the excess melt signal, and the eustatic signal during MIS 5a, 5c, and 5e interglacials. For MIS 5a and 5c, we apply GIA corrections derived from Bruhel Point, California (~160 km south of the Trinidad coastal area and closest reported value), of –8 to –14 m and –2 to –7 m, respectively (Creveling et al., 2017). For MIS 5e, we apply a GIS correction derived from San Nicholas Island, California, (~950 km south of the Trinidad coastal area and the closest reported value), of 10.91–13.01 m (Creveling et al., 2015). These paleo–highstand elevation estimates are similar to highstand estimates for northern California reported by Simms et al. (2016).

We quantify Late Pleistocene uplift rates for the Trinidad coastal area, which addresses a geospatial gap in Late Pleistocene coastal rock uplift rates within southern Cascadia. The maximum uplift rates in the Trinidad coastal area for surfaces 1–4 (MIS 5a, 5c, 5e, and 7) are 0.61, 0.82, 0.99, and 1.05 m/k.y., respectively (Table 3). The Trinidad fault daylights across surface 2 (106 ka) northeast

TABLE 2. THICKNESS OF COVER BED SEDIMENT ON SHORE PLATFORMS, NORTHERN CALIFORNIA (CA) TO SOUTHERN OREGON (OR) (USA)

Age of terrace: MIS* (approximate age [ka])	Crescent City, CA, thickness of cover bed sediment above shore platform (m)†	Brookings, OR, thickness of cover bed sediment above shore platform (m)§	Cape Blanco, OR, thickness of cover bed sediment above shore platform (m)#	Cape Arago, OR, thickness of cover bed sediments above shore platform (m)**	Average of minimums (to nearest m)	Average of maximums (to nearest m)
5a (ca. 80 ka)	N.D.	7.5 (n = 1)	6.4–9.0	3.0–20.0	5.6	12.2
5c (ca. 105 ka)	N.D.	2.0–12.0 (n = 2)	16.5–23.0	4.0–20.0	7.5	18.3
5e (ca. 125 ka)	3.0–15.0	4.0–12.0 (n = 3)	20.0–35.0	3.0–18.0	7.5	20.0
7 (?) (ca. 200 ka)	N.D.	6.0–13.0 (n = 5)	30.0–40.0	3.0–16.0	12.0	23.0

Note: N.D.—no data. Average of minimums to nearest tenth of a meter; average of maximums to nearest tenth of a meter.
*Marine isotope stage (Shackleton and Opdyke, 1973; Chappell and Shackleton, 1986).
†Polenz and Kelsey (1999).
§Kelsey and Bockheim (1994).
#Kelsey (1990).
**McInelly and Kelsey (1990).

TABLE 3. CALCULATION OF UPLIFT RATES FOR MARINE TERRACES ALONG TRANSECT X-X′, TRINIDAD COASTAL AREA, CALIFORNIA (USA)

Terrace number*	Surface elevation inner edge of terrace along transect X-X′ (m)†	Cover sediment thickness for sediment above platform inner edge (platform strath underlies terrace) (m)§	Elevation of platform inner edge (m)#	Indicative range of a Trinidad marine terrace (m)@	Paleo-highstand when platform was cut (max/min) (m)**	Amount of surface uplift (max/min) (m)††	Age of platform (ka)§§	Uplift rate (m/k.y.)##
1	40	5.6	34.4	+2.55	–8	44.95	84	0.54
					–14	50.95	84	0.61
				–2.55	–8	39.85	84	0.47
					–14	45.85	84	0.55
		12.2	27.8	+2.55	–8	38.35	84	0.46
					–14	44.35	84	0.53
				–2.55	–8	33.25	84	0.40
					–14	39.25	84	0.47
2	85	7.5	77.5	+2.55	–2	82.05	106	0.77
					–7	87.05	106	0.82
				–2.55	–2	76.95	106	0.73
					–7	79.95	106	0.75
		18.3	66.7	+2.55	–2	71.25	106	0.67
					–7	76.25	106	0.72
				–2.55	–2	66.15	106	0.62
					–7	71.15	106	0.67
3	140	7.5	132.5	+2.55	10.91	124.14	125	0.99
					13.01	122.04	125	0.97
				–2.55	10.91	119.04	125	0.95
					13.01	116.94	125	0.93
				+2.55	10.91	111.14	125	0.89
					13.01	109.04	125	0.87
				–2.55	10.91	106.04	125	0.85
					13.01	103.94	125	0.83
4	210	12	198	+2.55	0?	200.55	190	1.05
				–2.55	0?	195.45	190	1.03
				+2.55	0?	200.55	200	1.0
				–2.55	0?	195.45	200	0.98
		23	187	+2.55	0?	189.55	190	1.0
				–2.55	0?	184.45	190	0.97
				+2.55	0?	189.55	200	0.95
				–2.55	0?	184.45	200	0.92

*Terrace surfaces are numbered in order of elevation, from low to high.
†Surface elevation based on lidar digital elevation model (Figs. 11 and 14).
§See Table 2 for thickness of cover bed sediment on shore platforms. In order to incorporate the range of cover sediment thickness variability, we account for both maximum and minimum thickness estimates on separate rows.
#Elevation of inner edge calculated as the surface elevation minus estimated cover sediment thickness.
@The indicative range of a marine terrace inner edge along the Trinidad coastal area is 5.1 m (see text for explanation). Therefore, we account for the maximum and minimum elevation range of formation on separate rows.
**Paleo-highstand elevation when platform was cut (Creveling et al., 2015, 2017). We account for the full range of sea-level highstand elevation estimates by separating the maximum (max) and minimum (min) values on separate rows. See text for explanation.
††Amount of surface uplift calculated as the elevation of the platform inner edge plus the indicative range and minus the elevation of the paleo-highstand elevation estimates. We carry through the maximum (max) and minimum (min) calculated values.
§§Ages of platforms are based on the assignment of terrace platform 3 to be 125 ka. For terrace 4, we calculate the minimum and maximum ages on separate rows (Martinson et al., 1987) per the sediment cover thickness estimate. See text for explanation.
##Uplift rate calculated as amount of surface uplift divided by the age of the platform.

of Trinidad (Figs. 11–15). Surface 1 is on the footwall (down-dropped side) of the Trinidad fault, which accounts for the observation that surface 1 has the lowest long-term maximum uplift rate.

Evolution of the Trinidad Fault-Propagation Fold and Constraints on Upper-Plate Shortening

Carver and Burke (1992) first inferred fault-propagation folding within the Mad River fault zone based on forelimb dip of folds later cut by faults. Similarly, the Trinidad fault truncates the seaward-dipping forelimb of the Trinidad anticline (Figs. 11–15). Propagation of the fault below the surface buckles the material overlying the tip of the fault, that is, terrace surfaces 2, 3, 4, and 5. On the forelimb, older surfaces show more tilt and more anticlinal deformation. Progressive tilt with time is exemplified both by the progressively increasing seaward tilt of platforms 2, 3, and 4 in cross section (Fig. 15) and by an exposure at Agate Beach north of Patrick's Point (located on the eastern limb of the Trinidad anticline) where MIS 5e marine sediment is tilted more than MIS 5c marine sediment, which was deposited on an erosional unconformity above the underlying MIS 5e sediment (Fig. 10). Once the Trinidad fault ruptured surface 2 (Figs. 11–15), slip could be accommodated across the fault plane to the ground surface, and folding of the hanging-wall anticline ceased or became minor compared to contraction accommodated by slip on the fault.

We estimate a minimum horizontal shortening across the Trinidad anticline using a marine terrace surface. We assume that the forelimb of the Trinidad anticline steepens in response to propagation at depth of a fault tip of a reverse fault. In the forelimb region, the horizontal shortening due to fault slip can be estimated from the amount of seaward tilting resulting from fault tip propagation. We employ marine terrace 4, which we infer was formed at 195 ± 5 ka. Marine terrace 4 tilted seaward at the location of cross section Z-Z′ where the terrace is folded across the anticline crest (Figs. 11 and 16), from time of formation at 195 ± 5 ka until the time that the Trinidad fault broke the ground surface. The time that the fault broke the ground surface was after marine terrace 2 formed at 106 ka, because marine terrace 2 is cut by the fault and is not tilted seaward. Therefore, the interval of seaward tectonic tilting of marine terrace surface 4 is ~100 ± 6 k.y. in duration, the time period being from 195 ± 5 ka (time of formation of terrace 4) to shortly before or after 100 ka, which is the time that the fault broke the surface and also the time that we infer that slip propagation ceased to drive seaward tilting of terrace 4.

We estimate shortening of marine terrace surface 4 by first assuming that the original slope at the time of formation of a marine terrace is 15 m/km (Bradley and Griggs, 1976). Second, we compare horizontal length differences of the strath terrace platform before and after tectonically induced seaward tilting, that is, original seaward slope versus terrace tilt when the anticline ceased growing (Fig. 16B). To make a direct measurement of total horizontal shortening, we keep the inner edge stationary as a point of reference (Fig. 16B). The uplifted and tilted terrace is shown relative to the inner edge because both the terrace slope of formation and the imposed tectonic tilt must be fixed to the inner edge reference in order to graphically compute horizontal shortening. Based on deformation of terrace 4 at cross section location Y-Y′, the total amount of horizontal shortening caused by growth of the hanging wall anticline is 40 ± 5 m (Fig. 16B). The error of ±5 m is a conservative estimate based on the accuracy of the graphical measurement approach.

Tilt of the forelimb of the Trinidad anticline permits estimation of the minimum rate of horizontal shortening in the late Quaternary, which can be compared to the Holocene horizontal shortening rate derived from paleoseismic studies. The rate of horizontal shortening is the shortening length divided by the time over which the shortening took place. For the Trinidad anticline, given uncertainties in shortening length and elapsed time of shortening (40 ± 5 m; 100 ± 6 k.y.), the range in rate of horizontal shortening in the late Quaternary is 0.33–0.47 m/k.y. This rate is a minimum for shortening rate on the Trinidad anticline during the 100 ± 6 k.y. time period because we are just calculating shortening in the forelimb region, and there was additional shortening in the back-limb region, although the hanging-wall anticline is asymmetric with more shortening in the steeper forelimb. The late Quaternary horizontal shortening rate can be compared to a Holocene shortening rate derived from the published Holocene slip rate (0.2–0.4 m/k.y.) from paleoseismic studies of the Trinidad fault (Woodward-Clyde Consultants, 1980). Assuming the Trinidad fault dips 30°–40°, the above slip rate is equivalent to a Holocene shortening rate of 0.17–0.35 m/k.y., which overlaps the minimum late Quaternary shortening rate from analysis of forelimb tilt of the Trinidad anticline.

Assuming that the same late Quaternary minimum horizontal shortening rate continued to the present, then over the last 200,000 yr, shortening across the Trinidad anticline has been, at a minimum, 94 m. Considering that the convergence velocity of the Gorda–Juan de Fuca plate with respect to stable North America at the latitude of the Trinidad anticline (41°N) is 34 mm/yr (Wang et al., 2003) and that horizontal convergence (i.e., horizontal shortening) across the Trinidad anticline is, at a minimum, 0.47 mm/yr, we infer that at least a few percent of the strain accumulated on the Cascadia subduction zone during each subduction-zone-earthquake deformation cycle is converted to permanent deformation of the upper-plate Trinidad fault and Trinidad anticline.

Because surface uplift has affected both the hanging wall and the footwall of the Trinidad fault, there must be an underlying deeper fault, the hanging wall of which contains the entire Trinidad fault. Seismic reflection interpretations of Clarke (1992) depict the Trinidad fault splay rooting into a master thrust at depth. The Trinidad fault may be a splay off of the subduction zone megathrust, or a splay off of the master fault of the Mad River fault zone, which in turn is a splay of the subduction zone megathrust.

CONCLUSION

High-resolution lidar imagery of the marine terraced coastal region near Trinidad, California, has enabled meter-scale mapping of late Quaternary deposits

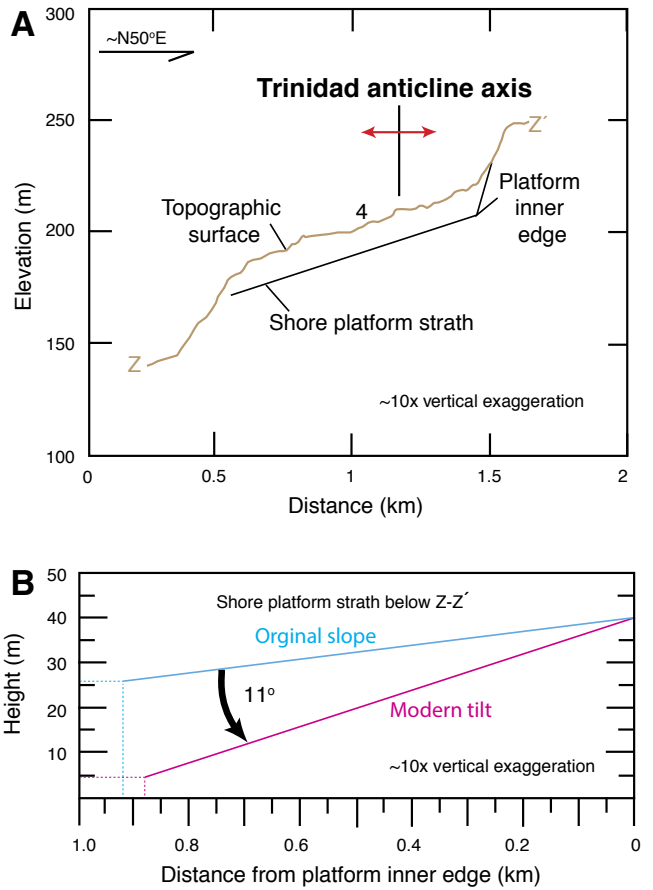

Figure 16. Northeast-trending topographic profile Z-Z′ (see location in Fig. 11) from which shortening rates were measured graphically. (A) Marine terrace 4 topographic surface and underlying shore platform. (B) Deformation of terrace surface 4 shore platform.

as well as faults and folds in the upper plate of the Cascadia subduction zone. We provide Late Pleistocene uplift and shortening rates, which fill a geospatial gap within the neotectonic and coastal geomorphology literature and also supplement understanding of southern Cascadia tectonic hazards. A surface classification method housed in a GIS (Bowles and Cowgill, 2012) serves as an objective measure for terrace mapping in lidar data sets. Five uplifted marine terraces collectively define the geometry of the Trinidad anticline that developed in the hanging wall of the Trinidad fault. Age assignments for marine terraces, which span 84 ka to >200 ka, are inferred based on inner-edge geomorphology and are consistent with soil development observations. The Trinidad anticline is a fault-propagation fold that ceased to be active when the associated reverse fault, the Trinidad fault, daylighted to the surface ca. 94–106 ka. Using paleo–sea level elevations to estimate the original elevation of the terraces, we calculate the average maximum uplift rates in the Trinidad coastal area to be ~1.0 m/k.y., and determine that the average long-term uplift rate diminishes westward to ~0.5–0.6 m/k.y. on the downthrown side of the Trinidad fault.

Minimum shortening across the north-northwest–trending Trinidad anticline in the last ~200 k.y. is ~94 m, with a minimum shortening rate approaching 0.5 m/k.y. For the last 200 k.y., Trinidad anticline contraction can account for upwards of at least 2% of the convergence of the Gorda–Juan de Fuca plate relative to a stable North America.

Because both the hanging wall and the footwall of the Trinidad fault have experienced surface uplift in the late Quaternary, it is not unreasonable to infer that the Trinidad fault and the associated fault propagation fold are in the hanging wall of a yet structurally lower thrust fault that roots in the subduction zone.

ACKNOWLEDGMENTS

Padgett received funding from a Humboldt State University, Geology Department, Raymond "Bud" Burke scholarship. We thank Joe Seney, the Arcata, California, USDA Soil Survey office and Raymond Burke for sharing soil description and lab data as well as insight into soil characteristics and classification. We also thank Tom Leroy, Sue Cashman, Mark Hemphill-Haley, and the Humboldt State University Geology Department for providing valuable insight and encouragement. Field assistance was provided by Celina Weeg, Laurel Hoffman, Erin Quinn, Heath Sawyer, Kelly Morgan, Chris Muhl, and Ian Pierce. Access permissions were provided by Green Diamond Resource Company, Danny Hagans, and Jeff Barnard. We thank Science Editor Shanaka de Silva for overseeing science review. We also thank Associate Editor Colin Amos, two anonymous reviewers, and Gina Harlow for their time and insight, which substantially improved the article. This is a contribution to International Geoscience Program-639 (IGCP-639) (Sea-level change from minutes to millennia).

REFERENCES CITED

Allan, J.C., and Komar, P.D., 2006, Climate controls on US West Coast erosion processes: Journal of Coastal Research, p. 511–529, https://doi.org/10.2112/03-0108.1.

Amos, C.B., Burbank, D.W., Nobes, D.C., and Read, S.A., 2007, Geomorphic constraints on listric thrust faulting: Implications for active deformation in the Mackenzie Basin, South Island, New Zealand: Journal of Geophysical Research, v. 112, B03S11, https://doi.org/10.1029/2006JB004291.

Anderson, R.S., Densmore, A.L., and Ellis, M.A., 1999, The generation and degradation of marine terraces: Basin Research, v. 11, p. 7–19, https://doi.org/10.1046/j.1365-2117.1999.00085.x.

Birkeland, P.W., 1984, Soils and Geomorphology: New York, Oxford University Press, 372 p.

Bowles, C.J., and Cowgill, E., 2012, Discovering marine terraces using airborne LiDAR along the Mendocino-Sonoma coast, northern California: Geosphere, v. 8, p. 386–402, https://doi.org/10.1130/GES00702.1.

Bradley, W.C., and Griggs, G.B., 1976, Form, genesis and deformation of central California wave-cut platforms: Geological Society of America Bulletin, v. 87, p. 433–449, https://doi.org/10.1130/0016-7606(1976)87<433:FGADOC>2.0.CO;2.

Burke, R.M., and Birkeland, P.W., 1979, Re-evaluation of multi-parameter relative dating techniques and their application to the glacial sequence along the eastern escarpment of the Sierra Nevada, California: Quaternary Research, v. 11, p. 21–51, https://doi.org/10.1016/0033-5894(79)90068-1.

Carver, G.A., and Burke, R.M., 1992, Late Cenozoic deformation on the Cascadia subduction zone in the region of the Mendocino triple junction, *in* Carver, G.A., and Burke, R.M., eds., Pacific Cell, Friends of the Pleistocene Guidebook for the Field Trip to Northern Coastal California: Arcata, California, Pacific Cell, Friends of the Pleistocene, p. 31–63.

Carver, G.A., Stephens, T.A., and Young, J.C., 1983, Quaternary thrust and reverse faulting on the Mad River fault zone, coastal northern California: Geological Society of America Abstracts with Programs, v. 15, no. 5, p. 316.

Carver, G.A., Burke, R.M., and Kelsey, H.M., 1985, Quaternary deformation studies in the region of the Mendocino triple junction, *in* Jacobson, M.L., and Rodriguez, T.R., compilers, National Earthquake Hazards Reduction Program: Summaries of Technical Reports, Volume XXI: U.S. Geological Survey Open-File Report 86-31, p. 58–62.

Chappell, J., and Shackleton, N.J., 1986, Oxygen isotopes and sea level: Nature, v. 324, p. 137–140, https://doi.org/10.1038/324137a0.

Clarke, S.H., Jr., 1992, Geology of the Eel River basin and adjacent region: Implications for late Cenozoic tectonics of the southern Cascadia subduction zone and Mendocino triple junction: American Association of Petroleum Geologists Bulletin, v. 76, p. 199–224.

Clarke, S.H., Jr., and Carver, G.A., 1992, Late Holocene tectonics and paleoseismicity, southern Cascadia subduction zone: Science, v. 255, p. 188–192, https://doi.org/10.1126/science.255.5041.188.

Creveling, J.R., Mitrovica, J.X., Hay, C.C., Austermann, J., and Kopp, R.E., 2015, Revisiting tectonic corrections applied to Pleistocene sea-level highstands: Quaternary Science Reviews, v. 111, p. 72–80, https://doi.org/10.1016/j.quascirev.2015.01.003.

Creveling, J.R., Mitrovica, J.X., Clark, P.U., Waelbroeck, C., and Pico, T., 2017, Predicted bounds on peak global mean sea level during marine isotope stages 5a and 5c: Quaternary Science Reviews, v. 163, p. 193–208, https://doi.org/10.1016/j.quascirev.2017.03.003.

Erslev, E.A., 1991, Trishear fault-propagation folding: Geology, v. 19, p. 617–620, https://doi.org/10.1130/0091-7613(1991)019<0617:TFPF>2.3.CO;2.

Frankel, K.L., and Dolan, J.F., 2007, Characterizing arid alluvial fan surface roughness with airborne laser swath mapping digital topographic data: Journal of Geophysical Research, v. 112, F02025, https://doi.org/10.1029/2006JF000644.

Kelsey, H.M., 1990, Late Quaternary deformation of marine terraces on the Cascadia subduction zone near Cape Blanco, Oregon: Tectonics, v. 9, p. 983–1014, https://doi.org/10.1029/TC009i005p00983.

Kelsey, H.M., and Bockheim, J.G., 1994, Coastal landscape evolution as a function of eustasy and surface uplift rate, Cascadia margin, southern Oregon: Geological Society of America Bulletin, v. 106, p. 840–854, https://doi.org/10.1130/0016-7606(1994)106<0840:CLEAAF>2.3.CO;2.

Kelsey, H.M., and Carver, G.A., 1988, Late Neogene and Quaternary tectonics associated with the northward growth of the San Andreas transform fault, northern California: Journal of Geophysical Research, v. 93, p. 4797–4819, https://doi.org/10.1029/JB093iB05p04797.

Kelsey, H.M., Ticknor, R.L., Bockheim, J.G., and Mitchell, E., 1996, Quaternary upper plate deformation in coastal Oregon: Geological Society of America Bulletin, v. 108, p. 843–860, https://doi.org/10.1130/0016-7606(1996)108<0843:QUPDIC>2.3.CO;2.

Lajoie, K.R., 1986, Coastal tectonics, *in* Wallace, R.E., ed., Active Tectonics: Washington, D.C., National Academy Press, p. 95–124.

Martinson, D.G., Pisias, N.G., Hays, J.D., Imbrie, J., Moore, T.C., and Shackleton, N.J., 1987, Age dating and the orbital theory of the ice ages: Development of a high-resolution 0 to 300,000-year chronostratigraphy: Quaternary Research, v. 27, p. 1–29, https://doi.org/10.1016/0033-5894(87)90046-9.

McInelly, G.W., and Kelsey, H.M., 1990, Late Quaternary tectonic deformation in the Cape Arago–Bandon region of coastal Oregon as deduced from wave-cut platforms: Journal of Geophysical Research, v. 95, p. 6699–6713, https://doi.org/10.1029/JB095iB05p06699.

McLaughlin, R.J., Ellen, S.D., Blake, M.C., Jr., Jayko, A.S., Irwin, W.P., Aalto, K.R., Carver, G.A., and Clarke, S.H., Jr., 2000, Geology of the Cape Mendocino, Eureka, Garberville, and southwestern part of the Hayfork 30 × 60 minute quadrangles and adjacent offshore area, northern California: U.S. Geological Survey Miscellaneous Field Studies MF-2336, 6 sheets scale 1:100,000, with 26 p. text.

Merritts, D., and Bull, W.B., 1989, Interpreting Quaternary uplift rates at the Mendocino triple junction, northern California, from uplifted marine terraces: Geology, v. 17, p. 1020–1024, https://doi.org/10.1130/0091-7613(1989)017<1020:IQURAT>2.3.CO;2.

Muhs, D.R., Kelsey, H.M., Miller, G.H., Kennedy, G.L., Whelan, J.F., and McInelly, G.W., 1990, Age estimates and uplift rates for the Late Pleistocene marine terraces: Southern Oregon portion of the Cascadia forearc: Journal of Geophysical Research, v. 95, p. 6685–6698, https://doi.org/10.1029/JB095iB05p06685.

Muhs, D.R., Simmons, K.R., Kennedy, G.L., and Rockwell, T.K., 2002, The last interglacial period on the Pacific Coast of North America: Timing and paleoclimate: Geological Society of America Bulletin, v. 114, p. 569–592, https://doi.org/10.1130/0016-7606(2002)114<0569:TLIPOT>2.0.CO;2.

Polenz, M., and Kelsey, H.M., 1999, Development of a late Quaternary marine terraced landscape during on-going tectonic contraction, Crescent City coastal plain: Quaternary Research, v. 52, p. 217–228, https://doi.org/10.1006/qres.1999.2061.

Rovere, A., Raymo, M.E., Vacchi, M., Lorscheid, T., Stocchi, P., Gómez-Pujol, L., Harris, D.L., Casella, E., O'Leary, M.J., and Hearty, P.J., 2016, The analysis of Last Interglacial (MIS 5e) relative sea-level indicators: Reconstructing sea-level in a warmer world: Earth-Science Reviews, v. 159, p. 404–427, https://doi.org/10.1016/j.earscirev.2016.06.006.

Ruggiero, P., Komar, P.D., and Allan, J.C., 2010, Increasing wave heights and extreme value projections: The wave climate of the US Pacific Northwest: Coastal Engineering, v. 57, p. 539–552.

Shackleton, N.J., and Opdyke, N.D., 1973, Oxygen isotope and paleomagnetic stratigraphy of equatorial Pacific core V28-238: Oxygen isotope temperatures and ice volumes on a 10^5 and 10^6 year time scale: Quaternary Research, v. 3, p. 39–55, https://doi.org/10.1016/0033-5894(73)90052-5.

Simms, A.R., Rouby, H., and Lambeck, K., 2016, Marine terraces and rates of vertical tectonic motion: The importance of glacio-isostatic adjustment along the Pacific coast of central North America: Geological Society of America Bulletin, v. 128, p. 81–93, https://doi.org/10.1130/B31299.1.

Stirling, C.H., Esat, T.M., Lambeck, K., and McCulloch, M.T., 1998, Timing and duration of the Last Interglacial: Evidence for a restricted interval of widespread coral reef growth: Earth and Planetary Science Letters, v. 160, p. 745–762, https://doi.org/10.1016/S0012-821X(98)00125-3.

Suppe, J., 1985, Principles of Structural Geology: Saddle River, New Jersey, Prentice Hall, Inc., 537 p.

Suppe, J., and Medwedeff, D.A., 1990, Geometry and kinematics of fault-propagation folding: Eclogae Geologicae Helvetiae, v. 83, no. 3, p. 409–454.

Tillotson, K., and Komar, P.D., 1997, The wave climate of the Pacific Northwest (Oregon and Washington): A comparison of data sources: Journal of Coastal Research, v. 13, p. 440–452.

USDA–NRCS (U.S. Department of Agriculture, Natural Resources Conservation Service), 2018, Soil survey of northern Humboldt and Del Norte Counties, California, https://websoilsurvey.sc.egov.usda.gov/app/WebSoilSurvey.aspx.

Wang, K., Wells, R., Mazzotti, S., Hyndman, R.D., and Sagiya, T., 2003, A revised dislocation model of interseismic deformation of the Cascadia subduction zone: Journal of Geophysical Research, v. 108, p. 2026, https://doi.org/10.1029/2001JB001227.

Woodward-Clyde Consultants, 1980, Evaluation of the potential for resolving the geologic and seismic issues at the Humboldt Bay Power Plant Unit No. 3, Summary report and Appendices A through D, Appendix B, Summary of Exploration Locality Investigations: San Francisco, p. B29–B49.